Nano Research 2016, 9(6): 1813–1822
DOI 10.1007/s12274-016-1074-1
Research Article
ISSN 1998-0124
CN 11-5974/O4

Achieving excellent bandwidth absorption by a mirror growth process of magnetic porous polyhedron structures

Hualiang Lv[1,3], Haiqian Zhang[1], Jun Zhao[2], Guangbin Ji[1] (✉), and Youwei Du[4]

[1] *College of Materials Science and Technology, Nanjing University of Aeronautics and Astronautics, Nanjing 211100, China*
[2] *School of Chemical and Biomedical Engineering, Nanyang Technological University, Singapore 637459, Singapore*
[3] *School of Materials Sciences and Engineering, Nanyang Technological University, 50 Nanyang Avenue, Singapore 639798, Singapore*
[4] *National Laboratory of Solid State Microstructures, Nanjing University, Nanjing 210093, China*

Received: 10 January 2016
Revised: 3 March 2016
Accepted: 16 March 2016

KEYWORDS
symmetrical hexagonal cone structure, $Fe_2O_3/BaCO_3$, single crystal, porous magnetic absorber, effective frequency bandwidth

ABSTRACT

A symmetrical $Fe_2O_3/BaCO_3$ hexagonal cone structure having a height of 10 μm and an edge length of ~4 μm is reported, obtained using a common solvothermal process and a mirror growth process. Focused ion beam and high-resolution transmission electron microscopy techniques revealed that α-Fe_2O_3 was the single crystal feature present. Ba ions contributed to the formation of symmetrical structures exhibited in the final composites. Subsequently, porous magnetic symmetric hexagonal cone structures were used to study the observed intense electromagnetic wave interference. Electromagnetic absorption performance studies at 2–18 GHz indicated stronger attenuation electromagnetic wave ability as compared to other shapes such as spindles, spheres, cubes, and rods. The maximum absorption frequency bandwidth was at 7.2 GHz with a coating thickness d = 1.5 mm. Special structures and the absence of $BaCO_3$ likely played a vital role in the excellent electromagnetic absorption properties described in this research.

1 Introduction

Nanomaterials have received extreme attention in the fields of drug delivery, catalysis, sensing, and energy storage, because of their outstanding physical and chemical properties [1–4]. However, evidence reveals that the novel properties of a given material are strongly dependent on its morphology. In general, tunable morphologies can lead to large differences in crystal structure, specific surface area, and size. For instance, graphene is a promising energy material because of its large specific sheet structure [5]. The exposed high index faces in Pt_xCu_y hexapod structures lead to enhanced catalytic activity [6]. Likewise, the

Address correspondence to gbji@nuaa.edu.cn

exposed (012) and (104) planes in α-Fe_2O_3 nanotubes give rise to favorable catalytic activity [7]. However, synthesizing such well-defined structures is difficult, especially for three-dimensional (3D) shapes.

Hydrothermal approaches are considered efficient strategies for achieving a wide range of morphologies. The morphologies that result from such hydrothermal processes are primarily decided by morphology controlling agents such as surfactants and inorganic ions [8, 9]. For instance, flower-like $Co_{20}Ni_{80}$ and CuS hierarchical structures can be achieved through the use of cetyltrimethyl ammonium bromide (CTAB) as a morphology control agent [10, 11]. Although well-defined structures can be successfully obtained in this manner, the resultant material is of low purity because of leftover surfactant molecules. A similar route to control structure growth and obtain some target morphology is by using inorganic ions, which can avoid some of the aforementioned shortcomings. For example, Fe_2O_3 with ellipsoidal, worm and quasi-cubic shapes has been synthesized with the assistance of halide ions [12]. Spindle-like Fe_2O_3 was obtained using PO_4^{3-} as a morphology control agent [13]. These findings reveal that specific inorganic ions can promote the growth of one facet while simultaneously suppressing the growth of others. In this regard, research into Ba ions has been somewhere rare. Recently, a new discovery revealed that symmetric hexagonal cone nanostructures can be easily achieved using Ba^{2+} as a morphology control agent. Owning to the quick reaction with CO_2, numerous crystal nuclei can be generated in the form of $BaCO_3$, which provide beneficial conditions to grow and enlarge structures that rely on Fe^{3+} ions. Depending on the crystal growth behavior of $BaCO_3$, $Fe_2O_3/BaCO_3$ composites can present symmetric hexagonal cone shapes. Such a rare polyhedron structure has aroused extreme interests with regard to electromagnetic pollution. With the rapid development of wireless technologies in recent years, electromagnetic pollution has received considerable research attention, as unwanted electromagnetic waves are an emerging health concern.

Electromagnetic absorbers are a type of functional material that can absorb incident electromagnetic waves and transfer them into thermal energy, reducing electromagnetic interface [14, 15]. Serious electromagnetic wave pollution resulting from the use electronic equipment can be treated in this manner. Electromagnetic wave scattering effects are available techniques to improve attenuation. In general, complicated polyhedron structures are better suited for electromagnetic scattering [16]. A symmetric hexagonal cone structure with 12 faces is able to induce strong electromagnetic wave scattering, which is favorable for attenuating electromagnetic waves. In addition, if the scattering structure has a magnetic character, the attenuation ability will be further increased because of impedance matching and magnetic loss [17, 18]. Thus, in order to obtain magnetic symmetric hexagonal cone structures, α-Fe_2O_3 was reduced to Fe or Fe_3O_4 with the assistance of H_2 or $NaBH_4$. Additionally, reduced magnetic composites also present interesting porous features.

2 Experimental

2.1 Materials

Sodium borohydride ($NaBH_4$), nitrate barium ($Ba(NO_3)_2$), iron nitrate ($Fe(NO_3)_3$) and sodium hydroxide (NaOH) were purchased from Nanjing Chemical Reagent Co. Ethylene glycol (EG-200) was purchased from the Sinopharm Chemical Reagent Co. All regents were analytically pure and used without further purification.

2.2 Preparation of symmetrical hexagonal cone $Fe_2O_3/BaCO_3$ composites

10 mmol $Fe(NO_3)_3$ and 1 mmol $Ba(NO_3)_2$ were dissolved into a 40 mL solvent mixture containing 10 mL EG-200 and 30 mL distilled water (DI), and stirred for 20 min to form a clear solution. A 50-mmol-solution NaOH was then added into the mixing solution and stirred for 10 min. This mixed solution was transferred to a Teflon-lined stainless steel autoclave (100 mL) and heated at 220 ℃ for 24 h. Finally, the resultant precipitates were collected by centrifugation and dried in a vacuum oven at 60 ℃ for 24 h.

2.3 Synthesis of magnetic porous $Fe/BaCO_3$ and $Fe_3O_4/BaCO_3$ composites

$Fe/BaCO_3$ was obtained by a thermal treatment process in a mixed atmosphere (V_{H2}/V_{N2} = 1:9). The

temperature was set at 500 ℃ for 2 h with an increase rate of 1 ℃·min^{-1}. For the porous $Fe_3O_4/BaCO_3$ composite, 0.1 g $Fe_2O_3/BaCO_3$ and 10 mmol $NaBH_4$ were dissolved into 30 mL DI and stirred for 10 min. Afterward, the solution was transferred into a 50 mL Teflon-lined stainless steel autoclave and heated at 160 ℃ for 12 h. A black precipitate was collected by magnetic separation and washed with ethanol five times.

2.4 Characterization

Crystal structures were examined using powder X-ray diffraction (XRD, Bruker D8 ADVANCE X-ray diffractometer) with Cu Kα radiation (λ = 0.154178 nm at a 40 kV scanning voltage, 40 mA scanning current and a scan range from 20° to 70°). Field emission scanning electron microscopy (FESEM, A Hitachi S4800 type) and transmission electron microscopy (TEM, FEI Tecnai) were used to determine the morphology and size features. Atomic ratios of Ba/Fe were characterized using inductively coupled plasma (ICP, Optima DV5300). Chemical bonding was characterized using Fourier transform infrared spectroscopy (FT-IR, Perkin-Elmer IR spectrometer) using KBr pellets. A focused ion beam (FIB) system was used to extract α-$Fe_2O_3/BaCO_3$ flakes (FEI versa 3D). X-ray photoelectron spectroscopy (XPS) was employed with a PHI 5000 VersaProbe.

2.5 Electromagnetic parameters

S parameters (S11, S12, S21 and S22) were tested with an Agilent PNA N5224A vector network analyzer using the coaxial-line method. Samples were prepared by homogeneously mixing paraffin wax and the sample (mass ratio = 7:3) and then pressed into toroidal-shaped samples (Φ_{out} = 7.0 mm, Φ_{in} = 3.04 mm). From this, software on the Agilent PNA can calculate the ε', ε'', μ', and μ'' values. Finally, RL values at different thicknesses d can be calculated by inputting the electromagnetic parameters (ε', ε'', μ', μ'') into the following equations [19, 20]

$$Z_{in} = Z_o(\mu_r/\varepsilon_r)^{1/2}\tanh[j(2\pi fd(\mu_r\varepsilon_r)^{1/2}/c)] \quad (1)$$

$$RL(dB) = 20\log|(Z_{in}-Z_o)/(Z_{in}+Z_o)| \quad (2)$$

where Z_{in} is the input impedance of the absorber, f is the frequency of the electromagnetic radiation, d is the coating thickness of the absorber and c is the velocity of an electromagnetic wave in free space. ε_r ($\varepsilon_r = \varepsilon' - j\varepsilon''$) and μ_r ($\mu_r = \mu' - j\mu''$) are the complex permittivity and permeability of the absorber, respectively.

3 Results and discussion

3.1 Crystal structures and microstructures of $Fe_2O_3/BaCO_3$ and Fe_2O_3

In order to explore the influence of Ba ions on the final nanostructure, control samples were prepared without additional $Ba(NO_3)_2$. Crystal structures of the two products were characterized by XRD, as seen in Fig. 1(a). With no added $Ba(NO_3)_2$, the as-obtained diffraction peaks are well-matched with α-Fe_2O_3 standard peaks (JCPDS No.: 33-0664). No other

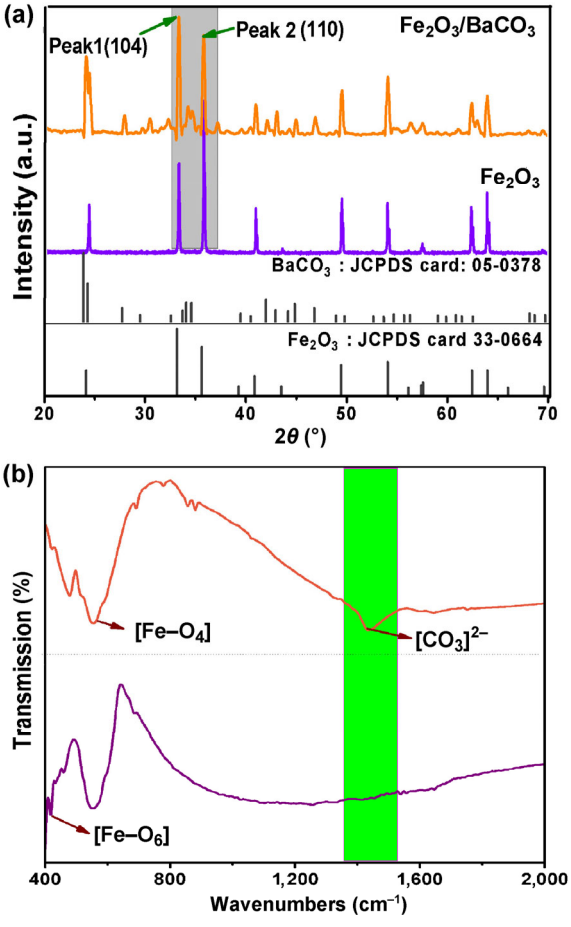

Figure 1 The XRD patterns (a) and FT-IR spectra (b) of Fe_2O_3 and $Fe_2O_3/BaCO_3$.

diffraction peaks were observed, indicating the high purity of the sample. Along with the Fe_2O_3 characteristic peaks, weak $BaCO_3$ diffraction peaks were detected when $Ba(NO_3)_2$ was added. However, Ba^{2+} seems to promote the growth of the (104) crystal plane as shown in the XRD pattern of the $Fe_2O_3/BaCO_3$ sample. Without Ba^{2+}, Fe_2O_3 instead prefers the (110) crystal plane, resulting in different microstructures. In addition, the formation of $BaCO_3$ can be explained that in alkaline solution, Ba ions are quickly converted to $Ba(OH)_2$ and then absorb CO_2 to form $BaCO_3$. Because of small amounts of $BaCO_3$ present, the XRD pattern is not as sharp as that of α-Fe_2O_3. FT-IR spectroscopy was also employed to obtain more information about CO_3^{2-} (Fig. 1(b)). Of note, Fe–O absorption peaks are apparent at 469 and 540 cm^{-1} that account for the stretching vibrations of FeO_4 tetrahedra and FeO_6 octahedra. Meanwhile, another new absorption peak at 1,423 cm^{-1} is present with additional $Ba(NO_3)_2$, which is ascribed to the presence of CO_3^{2-}. In addition, the atomic ratio of Ba/Fe is approximately 1.6, as determined by ICP.

FESEM and high-resolution TEM (HRTEM) images are shown in Fig. 2. The $Fe_2O_3/BaCO_3$ composite has a clear symmetric hexagonal cone structure, while Fe_2O_3 is present in a spindle-like shape (Figs. 2(a) and 2(h)). High-magnification images from different angles reveal symmetric hexagonal cones of $Fe_2O_3/BaCO_3$ having 12 smooth faces of ~4 μm on the side edge, 2 μm on the bottom edge, and 10 μm in height (Figs. 2(b)–2(d)). Such size features ensure strong electromagnetic wave scattering. FIB and HRTEM techniques have been conducted to confirm the existence of $BaCO_3$ in these structures (Figs. 2(e) and 2(f)), using a thin flak extracted from one cone structure. In Fig. 2(f), a lattice fringe distance d = 0.27 nm matches well with the (104) phase of α-Fe_2O_3. Another lattice fringe d = 0.44 nm is indexed to the (020) crystal phase of $BaCO_3$. Meanwhile, the selected area electron diffraction (SAED) map (green frame) demonstrates the single crystal features of α-Fe_2O_3 (Fig. 2(g)). In Figs. 2(h) and 2(i), we can infer that only spindle-like Fe_2O_3 ~1.5 μm in height is formed.

These large differences in microstructure are attributed to Ba ions.

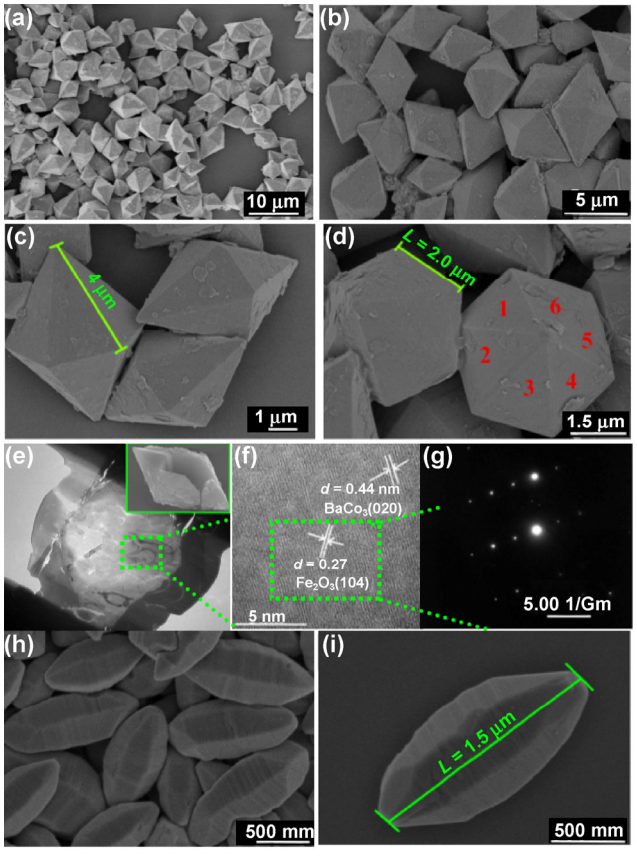

Figure 2 SEM images of the two products with $Ba(NO_3)_2$ ((a)–(d)), without $Ba(NO_3)_2$ ((h) and (i)); FIB image (e), HRTEM (f) and corresponding SAED image (g) of the sample prepared by adding $Ba(NO_3)_2$.

3.2 Self-assembly of symmetrical hexagonal cones

Time-dependent experiments are a powerful tool to explore the probable formation mechanisms of nanostructures. The formation involves a self-assembly process where high temperatures allow Ba^{2+} to rapidly react with OH^- and CO_2 to form $BaCO_3$ nuclei. Each $BaCO_3$ nucleus is surrounded by numerous of Fe ions, making them more inclined to form irregular $Fe_2O_3/BaCO_3$ nanosheets with uniform thickness of ~20 nm after 6 h of reaction time. Because of the high surface energy, these sheets can spontaneously stack and self-assemble into a larger sheet in order to decrease this surface energy. As can be seen in Fig. 3(b), larger flakes are present after 9 h of reaction time. Subsequently, these larger flakes further accumulate and result in irregular three-dimensional shapes with sharp top (Fig. 3(c)). After a reaction time of 12 h, the

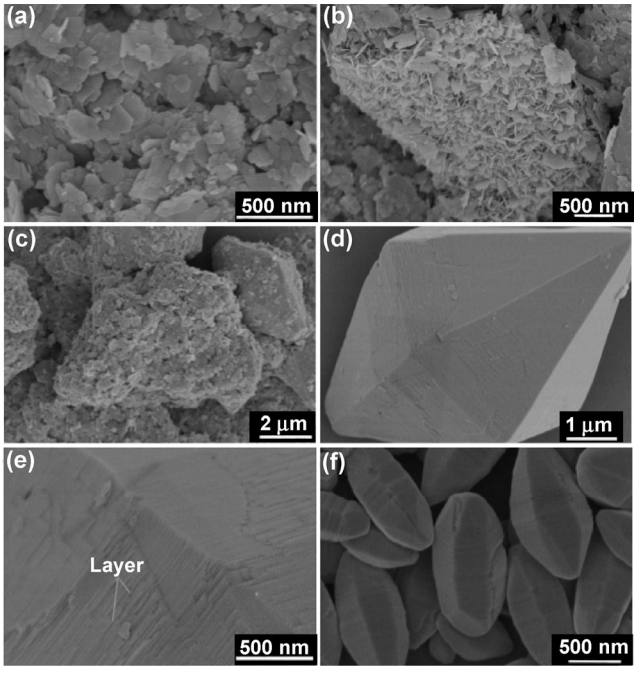

Figure 3 SEM images of the iron oxide prepared at different times (a) 6 h; (b) 9 h; (c) 12 h; (d)–(e) 18 h; (f) Fe_2O_3 prepared with adding $NaNO_3$.

surface is quite disordered and the interior is less dense. After another 6 h, the symmetrical hexagonal cone structures emerge (Fig. 3(d)). Each face of the conical structure is rough with apparent multi-layer features. Fe ions in solution, when adsorbed on a notched surface, induce a hydrolytic process to yield smooth surfaces. However, when less Ba^{2+} is present, many smaller hexagonal cones appear (Fig. S1 in the Electronic Supplementary Material (ESM)), indirectly indicating that a suitable amount of Ba^{2+} also can enlarge these conical structures. Unfortunately, excess amounts of Ba^{2+} do not ensure well-defined conical structures, and nanoflake and tube structures are also formed. During the crystal growth process, $BaCO_3$ nuclei aid the symmetrical formations, with aggregation into nanoflakes structures and subsequent self-assembly into tube structures (Figs. S2 and S3 in the ESM) because of its growth habits. To rule out the potential influence of NO_3^-, experiments were also performed by replacing $Ba(NO_3)_2$ with $NaNO_3$. The resulting structures did not show obvious changes, indicating that NO_3^- does not influence the final microstructure.

3.3 Phases and microstructures of porous Fe/$BaCO_3$ and Fe_3O_4/$BaCO_3$

In order to obtain magnetic Fe_3O_4/$BaCO_3$ and Fe/$BaCO_3$ cone structures, the as-prepared Fe_2O_3/$BaCO_3$ was reduced using H_2 or $NaBH_4$. Corresponding SEM images and XRD patterns are shown in Fig. 4. Two reduced composites retained the original symmetrical 12-faced cone shape. However, in contrast with the original shapes, the polyhedral Fe_3O_4/$BaCO_3$ composite cones are composed of numerous irregular particles ~300 nm in size (Figs. 4(a)–4(d)). These large particles are part of a crystal re-growth process which Fe^{3+} ions can be reduced to Fe^{2+} by $NaBH_4$. Fe_3O_4 is formed by the re-combination of Fe^{2+}, Fe^{3+}, and O^{2-} ions, leading to porous features. Although porous features are also present in the Fe/$BaCO_3$ composite, the formation mechanism is different. During the heated treatment

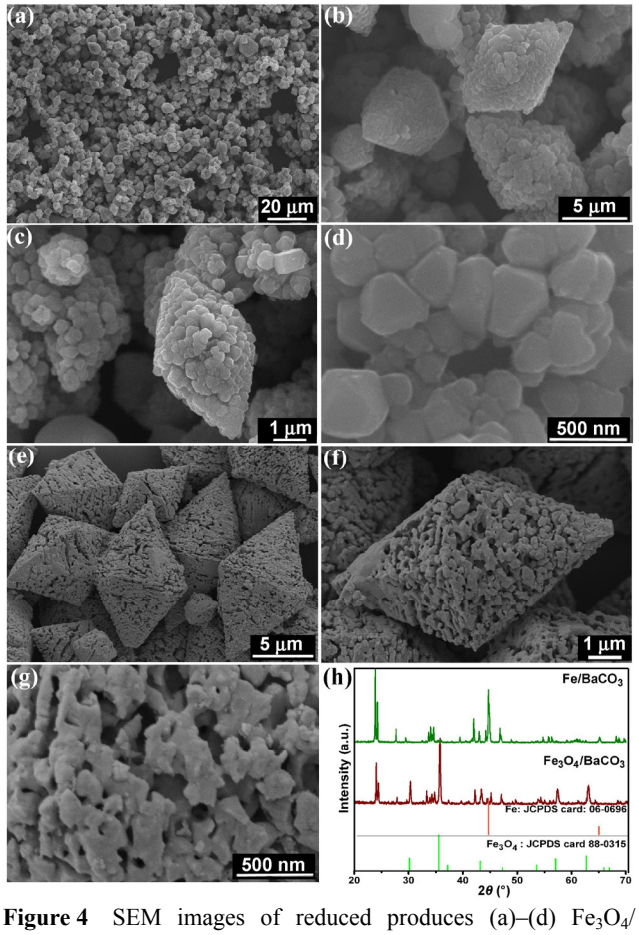

Figure 4 SEM images of reduced produces (a)–(d) Fe_3O_4/$BaCO_3$; (e)–(g) Fe/$BaCO_3$; (h) XRD patterns of Fe_3O_4/$BaCO_3$ and Fe/$BaCO_3$.

process, O^{2-} is consumed to form water vapor with H_2 (Figs. 4(e)–4(g)), and this vapor can lead to porous structures. XRD patterns of two reduced products are shown in Fig. 4(h). The original Fe_2O_3 diffraction peaks were replaced by α-Fe and Fe_3O_4. $BaCO_3$ characteristic peaks can still be observed as well, indicating the existence of Fe/$BaCO_3$ and Fe_3O_4/$BaCO_3$ composites. The existence of Fe and Fe_3O_4 also can be proven with XPS data, as displayed in Figs. S4 and S5 (in the ESM). In the Fe/$BaCO_3$ sample, a binding energy of 709.4 eV denotes Fe. Because of the prolonged exposure to air, Fe_2O_3 peaks are also present. It should be noted that because of the amount of Fe_2O_3 present, the peak intensity of Fe_2O_3 is quite weak compared to Fe. In Fig. S5 (in the ESM), a binding energy of 711.4 eV is attributed to Fe_3O_4.

3.4 Microwave absorption properties of Fe/$BaCO_3$ and Fe_3O_4

For microwave absorption, a desirable absorber should have as broad a frequency region (f_E) as possible, with RL $\leqslant$ 10 dB corresponding to 90% of absorption and attenuation [21]. In this case, the coating of a given layer must be controlled within a small range. In other word, a strong absorber with a large d value (usually d < 2.0 mm) is not as useful as one might expect. Reflection loss value versus frequency curves at d = 1.5 mm are shown in Fig. 5. Figure 5(a) shows that the Fe_3O_4/$BaCO_3$ composite has a f_E value of 3.6 GHz (14.4–18 GHz) and a corresponding RL_{min} value of –28 dB. For Fe/$BaCO_3$, the f_E value is two times broader than that of Fe_3O_4/$BaCO_3$ and the optimal reflection loss value is larger than –20 dB (Fig. 5(b)). The f_E values of similar samples are shown in Figs. 5(c) and 5(d), demonstrating obvious improvements in these two samples [22–32].

In fact, to obtain highly effective electromagnetic absorption, the absorber should have a large impedance matching ratio (Z) to free space, which allows more electromagnetic wave incidence into the absorption layer and reduces unwanted reflection from the interface. Generally, Z can be expressed as [33]

$$Z = Z_1/Z_0 \quad (3)$$

$$Z_1 = (\mu_r/\varepsilon_r)^{1/2} Z_0 \quad (4)$$

where Z_1 is the impedance matching of the absorber, and Z_0 is the free space of impedance matching. The Z value of the Fe/$BaCO_3$ composite is >0.3 over the whole frequency range, while Fe_3O_4/$BaCO_3$ is smaller (0.1–0.15). It should be noted, however, that these Z values are larger than typical non-magnetic dielectric materials (<0.1). In the second stage, the incoming electromagnetic energy is converted to thermal energy depending on the magnetic or dielectric loss ability.

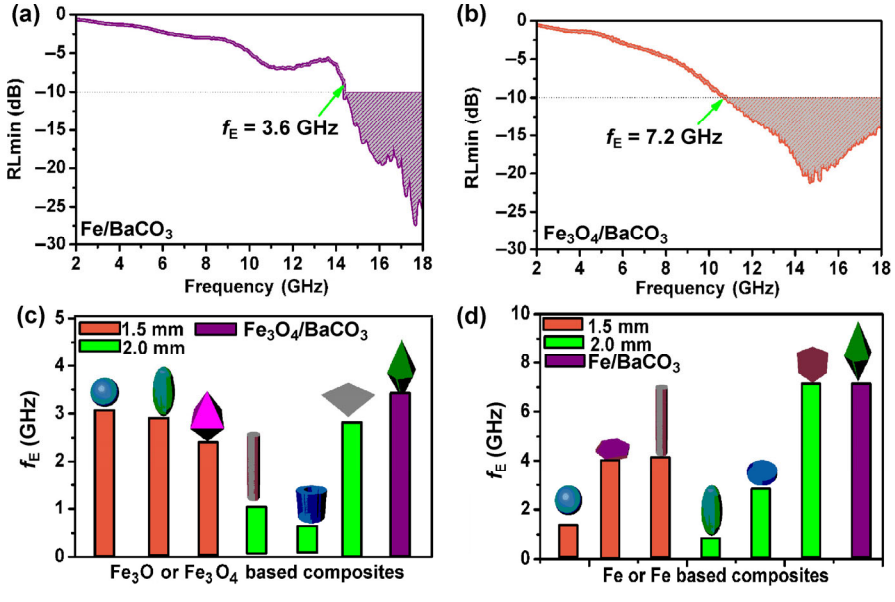

Figure 5 Reflection loss data of reduced composites: (a) Fe_3O_4/$BaCO_3$; (b) Fe/$BaCO_3$; (c) f_E value of similar Fe_3O_4 or based composites (d) f_E value of similar Fe or based composites.

The attenuation constant α describes the attenuation ability as [34]

$$\alpha = \frac{\sqrt{2}\pi f}{c} \times \sqrt{(\mu''\varepsilon'' - \mu'\varepsilon') + \sqrt{(\mu''\varepsilon'' - \mu'\varepsilon')^2 + (\mu'\varepsilon'' + \mu''\varepsilon')^2}} \quad (5)$$

It is worth noting that strong attenuation behavior of a material results from synergy between the magnetic and dielectric loss ability. In Fig. 6(b), the α values of two samples at high frequency exceed 100, indicating strong attenuation.

To better understand the probable dielectric or magnetic loss mechanisms, electromagnetic parameters are provided in Fig. 7. Generally, we regard the real part of the permittivity (ε') as the storage electric ability, while the imaginary part of permittivity (ε'') is the loss ability. Likewise, the real part of permeability μ' represents the storage magnetic ability and μ'' is related to the magnetic loss ability. In Fig. 7(a), ε' of $Fe/BaCO_3$ is slightly larger than that of $Fe_3O_4/BaCO_3$. At 2–18 GHz, the ε' values of two samples are <10, beneficial for impedance matching behavior. As for their dielectric loss ability, the porous $Fe/BaCO_3$ composite presents increased tendency at 5–18 GHz. An enhanced ε'' value for $Fe/BaCO_3$ indicates that incident electromagnetic energy can be easily consumed at high frequencies. Based on the 1/4 wavelength equation, a larger ε'' value at high frequency also leads to a smaller d value [35, 36]

$$d = nc/4f_m(\varepsilon_r\mu_r)^{1/2} \quad (6)$$

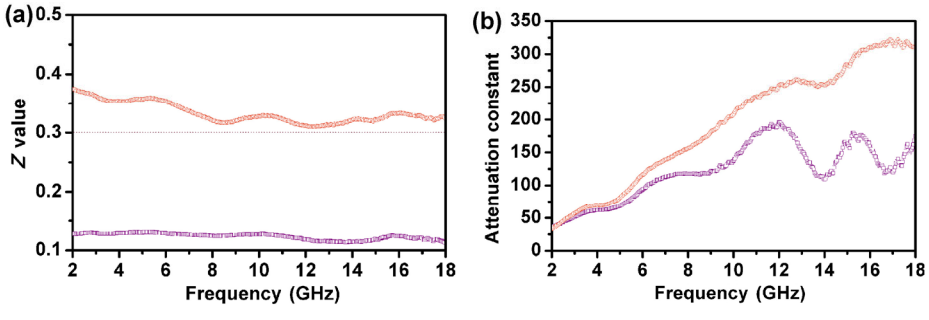

Figure 6 Impedance matching ratios (a) and attenuation constants of the two reduced products.

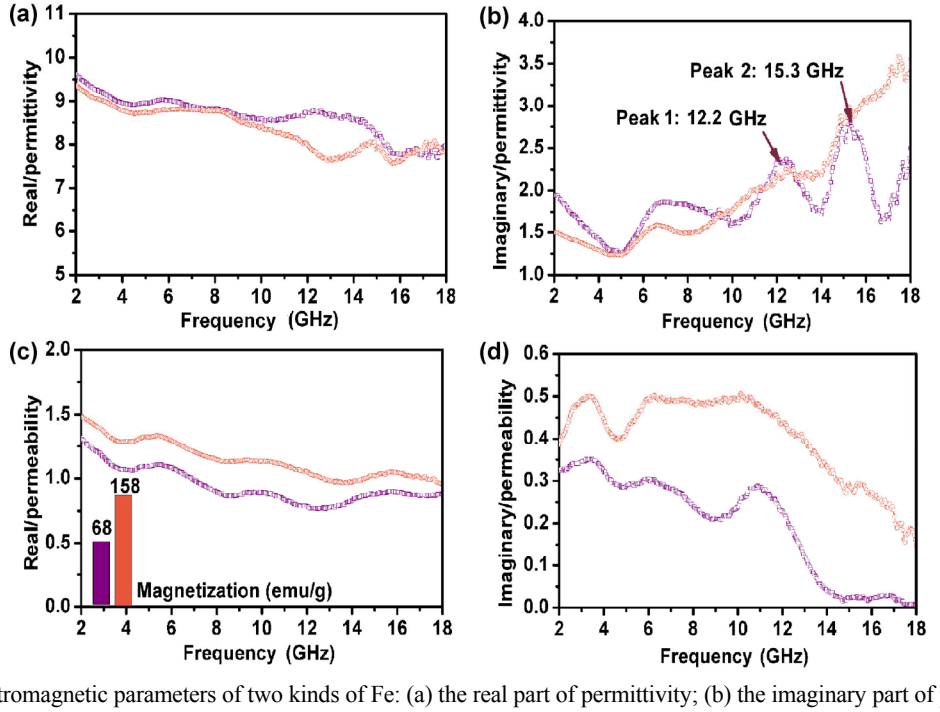

Figure 7 The electromagnetic parameters of two kinds of Fe: (a) the real part of permittivity; (b) the imaginary part of permittivity; (c) the real part of permeability; (d) the imaginary part of permeability.

In the $Fe_3O_4/BaCO_3$ composite, two obvious resonance peaks at 12.3 and 15.7 GHz are favorable for large ε'' values. The minimal presence of nanocrystalline $BaCO_3$ affects the dipole center of Fe and Fe_3O_4, resulting in dipole polarization which is reflected in an increased ε'' value. Special polyhedral structures also affect the novel dielectric loss behavior.

Magnetization values influence the final μ' and μ'' values. From the inset of Fig. 7(c), the magnetization value of $Fe/BaCO_3$ is approximately 158 emu·g^{-1}, superior to that of $Fe_3O_4/BaCO_3$ (68 emu·g^{-1}). Hence, $Fe/BaCO_3$ has larger μ' and μ'' values than $Fe_3O_4/BaCO_3$. However, the two samples do not share excellent magnetic loss ability because of these smaller μ'' values. Rather, these properties are ascribed to the novel porous symmetrical hexagonal cone structure. It is widely believed that magnetic materials always contain eddy current effects, which have a negative role on microwave absorption and can be expressed as [37]

$$C_0 = \mu'' (\mu')^{-2} f^{-1} = 2\pi\mu_0 d^2\delta \quad (7)$$

If the eddy current effect is present, C_0 will remain constant as the frequency increases. In Fig. 8, changes in C_0 are present in both samples, indicating that eddy currents are successfully suppressed by the porous cone structure.

Electromagnetic wave scattering is considered another vital aspect to increasing the attenuation ability of an absorber, as shown in Fig. 9. The transmission of electromagnetic wave may involve the following parts

$$\text{Attenuation } (A_1) = \text{Emission } (A_0) - \text{reflection } (A_2) - \text{penetration } (A_3)$$

Generally, most incident electromagnetic radiation will be attenuated by magnetic and dielectric loss (A_1). Nevertheless, a large portion of un-attenuated electromagnetic radiation can penetrate the absorption layer and spread into free space (denoted as A_3). Relying on the unique polyhedral structure, un-attenuated electromagnetic radiation has difficultly penetrating the coating layer because of intensity scattering effects. Porous structures also have better scattering effects.

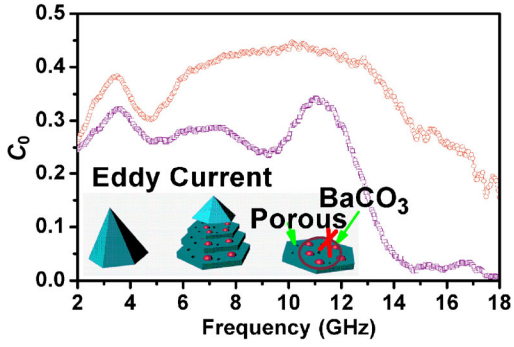

Figure 8 C_0 value of two samples.

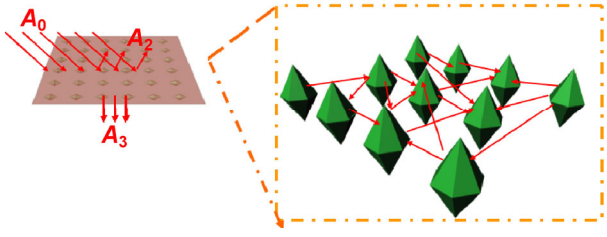

Figure 9 Schematic illustration of the electromagnetic wave scattering effect.

4 Conclusions

In this study, symmetric hexagonal cone structures were created using a mirror growth process, with Ba^{2+} playing a vital role on the final structure. The crystal growth process was discussed in detail. To obtain better electromagnetic absorption, magnetic porous $Fe/BaCO_3$ and $Fe_3O_4/BaCO_3$ samples were achieved by a second reduction process. With a small coating layer, both products attained larger f_E values, with a f_E value of 7.2 GHz for $Fe/BaCO_3$. The excellent microwave absorption can be attributed to the unique structure and the presence of $BaCO_3$.

Acknowledgements

Financial support from the National Natural Science Foundation of China (No. 11575085), the Aeronautics Science Foundation of China (No. 2014ZF52072), the Funding for Outstanding Doctoral Dissertation in NUAA (No. BCXJ15-09), the Open Research Fund of Jiangsu Provincial Key Laboratory for Nanotechnology of Nanjing University, and the Priority Academic Program Development of Jiangsu Higher Education Institutions is gratefully acknowledged.

Electronic Supplementary Material: Supplementary material (SEM images of samples prepared with different amount of $Ba(NO_3)_2$, XPS data of $Fe/BaCO_3$ and $Fe_3O_4/BaCO_3$) is available in the online version of this article at http://dx.doi.org/ 10.1007/s12274-016-1074-1.

References

[1] Zhang, K.; Hu, Z.; Liu, X.; Tao, Z. L.; Chen, J. $FeSe_2$ microspheres as a high-performance anode material for Na-ion batteries. *Adv. Mater*. **2015**, *27*, 3305–3309.

[2] Han, F.; Ma, L. J.; Sun, Q.; Lei, C.; Lu, A. H. Rationally designed carbon-coated Fe_3O_4 coaxial nanotubes with hierarchical porosity as high-rate anodes for lithium ion batteries. *Nano Res*. **2014**, *7*, 1706–1717.

[3] Chen, Y. M.; Li, Z.; Lou, X. W. D. General formation of $M_xCo_{3-x}S_4$ (M = Ni, Mn, Zn) hollow tubular structures for hybrid supercapacitors. *Angew. Chem., Int. Ed.* **2015**, *54*, 10521–10524.

[4] Guo, W. X.; Sun, W. W.; Wang, Y. Multilayer CuO@NiO hollow spheres: Microwave-assisted metalorganic-framework derivation and highly reversible structure-matched stepwise lithium storage. *ACS Nano* **2015**, *9*, 11462–11471.

[5] Park, S. H.; Kim, H. K.; Yoon, B. S.; Lee, C. W.; Ahn, D.; Lee, S. I.; Roh, K. C.; Kim, K. B. Spray-assisted deep-frying process for the *in situ* spherical assembly of graphene for energy-storage devices. *Chem. Mater*. **2015**, *27*, 457–465.

[6] Liu, Y. J.; Xin, F. X.; Zhu, E. B.; Chen, L.; Huang, Y.; Chen, C. F. Pt_xCu_y nanocrystals with hexa-pod morphology and their electrocatalytic performances towards oxygen reduction reaction. *Nano Res*. **2015**, *8*, 3342–3352.

[7] Wu, W.; Hao, R.; Liu, F.; Su, X. T.; Hou, Y. L. Single-crystalline α-Fe_2O_3 nanostructures: Controlled synthesis and high-index plane-enhanced photodegradation by visible light. *J. Mater. Chem. A* **2013**, ***1***, 6888–6894.

[8] Shen, L. F.; Yu, L.; Yu, X. Y.; Zhang, X. G.; Lou, X. W. D. Self-templated formation of uniform $NiCo_2O_4$ hollow spheres with complex interior structures for lithium-ion batteries and supercapacitors. *Angew. Chem., Int. Ed*. **2015**, *54*, 1868–1872.

[9] Lv, H. L.; Liang, X. H.; Ji, G. B.; Zhang, H. Q.; Du, Y. W. Porous three-dimensional flower-like Co/CoO and its excellent electromagnetic absorption properties. *ACS Appl. Mater. Interfaces* **2015**, *7*, 9776–9783.

[10] Liu, Q. H.; Xu, X. H.; Xia, W. X.; Che, R. C.; Chen, C.; Cao, Q.; He, J. G. Dependency of magnetic microwave absorption on surface architecture of $Co_{20}Ni_{80}$ hierarchical structures studied by electron holography. *Nanoscale* **2015**, *7*, 1736–1743.

[11] He, S.; Wang, G. S.; Lu, C.; Luo, X.; Wen, B.; Guo, L.; Cao, M. S. Controllable fabrication of CuS hierarchical nanostructures and their optical, photocatalytic, and wave absorption properties. *ChemPlusChem* **2013**, *78*, 250–258.

[12] Ma, R. G.; Wang, M.; Dam, D. T.; Dong, Y. C.; Chen, Y.; Moon, S. K.; Yoon, Y. J.; Lee, J. M. Halide-ion-assisted synthesis of different α-Fe_2O_3 hollow structures and their lithium-ion storage properties. *ChemPlusChem* **2015**, *80*, 522–528.

[13] Zhang, J. N.; Wang, K. X.; Xu, Q.; Zhou, Y. C.; Cheng, F. Y.; Gu, S. J. Beyond yolk–shell nanoparticles: Fe_3O_4@Fe_3C core@shell nanoparticles as yolks and carbon nanospindles as shells for efficient lithium ion storage. *ACS Nano* **2015**, *9*, 3369–3376.

[14] Ning, M. Q.; Lu, M. M.; Li, J. B.; Chen, Z.; Dou, Y. K.; Wang, C. Z.; Rehman, F.; Cao, M. S.; Jin, H. B. Two-dimensional nanosheets of MoS_2: A promising material with high dielectric properties and microwave absorption performance. *Nanoscale* **2015**, *7*, 15734–15740.

[15] Lv, H. L.; Ji, G. B.; Wang, M.; Shang, C. M.; Zhang, H. Q.; Du, Y. W. FeCo/ZnO composites with enhancing microwave absorbing properties: Effect of hydrothermal temperature and time. *RSC Adv*. **2014**, *4*, 57529–57533.

[16] Lv, H. L.; Liang, X. H.; Cheng, Y.; Zhang, H. Q.; Tang, D. M.; Zhang, B. S.; Ji, G. B.; Du, Y. W. Coin-like α-Fe_2O_3@$CoFe_2O_4$ core–shell composites with excellent electromagnetic absorption performance. *ACS Appl. Mater. Interfaces* **2015**, *7*, 4744−4750.

[17] Qiu, J.; Qiu, T. T. Fabrication and microwave absorption properties of magnetite nanoparticle–carbon nanotube–hollow carbon fiber composites. *Carbon* **2015**, *81*, 20–28.

[18] Chen, Y.; Wang, Y. L.; Zhang, H. B.; Li, X. F.; Gui, C. X.; Yu, Z. Z. Enhanced electromagnetic interference shielding efficiency of polystyrene/graphene composites with magnetic Fe_3O_4 nanoparticles. *Carbon* **2015**, *82*, 67–76.

[19] Najim, M.; Modi, G.; Mishra, Y. K.; Adelung, R.; Singh, D.; Agarwala, V. Ultra-wide bandwidth with enhanced microwave absorption of electroless Ni–P coated tetrapod-shaped ZnO nano- and microstructures. *Phys. Chem. Chem. Phys*. **2015**, *17*, 22923–22933.

[20] Zhao, B.; Fan, B. B.; Xu, Y. W.; Shao, G.; Wang, X. D.; Zhao, W. Y.; Zhang, R. Preparation of honeycomb SnO_2 foams and configuration-dependent microwave absorption features. *ACS Appl. Mater. Interfaces* **2015**, *7*, 26217–26225.

[21] Liu, Q. H.; Cao, Q.; Bi, H.; Liang, C. Y.; Yuan, K. P.; She, W.; Yang, Y. J.; Che, R. C. CoNi@SiO_2@TiO_2 and CoNi@Air@TiO_2 microspheres with strong wideband microwave absorption. *Adv. Mater*. **2016**, *28*, 486–490.

[22] Du, Y. C.; Liu, W. W.; Qiang, R.; Wang, Y.; Han, X. J.; Ma, J.; Xu, P. Shell thickness-dependent microwave absorption of

core−shell Fe_3O_4@C composites. *ACS Appl. Mater. Interfaces* **2014**, *6*, 12997–13006.

[23] Xu, J. J.; Liu, J. W.; Che, R. C.; Liang, C. Y.; Cao, M. S.; Li, Y.; Liu, Z. W. Polarization enhancement of microwave absorption by increasing aspect ratio of ellipsoidal nanorattles with Fe_3O_4 cores and hierarchical $CuSiO_3$ shells. *Nanoscale* **2014**, *6*, 5782–5790.

[24] Shang, C. M.; Ji, G. B.; Liu, W.; Zhang, X. M., Lv, H. L.; Du, Y. W. One-pot *in situ* molten salt synthesis of octahedral Fe_3O_4 for efficient microwave absorption application. *RSC Adv*. **2015**, *5*, 80450–80456.

[25] Yong, Y.; Yang, Y.; Wen, X.; Jun, D. Microwave electromagnetic and absorption properties of magnetite hollow nanostructures. *J. Appl. Phys*. **2014**, *115*, 17A521.

[26] Wang, L.; Huang, Y.; Sun, X.; Huang, H. J.; Liu, P. B.; Zong, M.; Wang, Y. Synthesis and microwave absorption enhancement of graphene@Fe_3O_4@SiO_2@NiO nanosheet hierarchical structures. *Nanoscale* **2014**, *6*, 3157–3164.

[27] Lv, H. L.; Ji, G. B.; Liu, W.; Zhang, H. Q.; Du, Y. W. Achieving hierarchical hollow carbon@Fe@Fe_3O_4 nanospheres with superior microwave absorption properties and lightweight features. *J. Mater. Chem. C* **2015**, *3*, 10232–10241.

[28] Fu, L. S.; Jiang, J. T.; Xu, C. Y.; Zhen, L. Synthesis of hexagonal Fe microflakes with excellent microwave absorption performance. *CrystEngComm* **2012**, *14*, 6827–6832.

[29] Lv, H. L.; Ji, G. B.; Liang, X. H.; Zhang, H. Q.; Du, Y. W. A novel rod-like MnO_2@Fe loading on graphene giving excellent electromagnetic absorption properties. *J. Mater. Chem. C* **2015**, *3*, 5056–5064.

[30] Lv, H. L.; Ji, G. B.; Zhang, H. Q.; Li, M.; Zuo, Z. Z.; Zhao, Y.; Zhang, B. S.; Tang, D. M.; Du, Y. W. Co_xFe_y@C composites with tunable atomic ratios for excellent electromagnetic absorption properties. *Sci. Rep*. **2015**, *5*, 18249.

[31] Lv, H. L.; Liang, X. H.; Cheng, Y.; Ji, G. B.; Tang, D. M.; Zhang, B. S.; Zhang, H. Q.; Du, Y. W. Facile synthesis of porous coin-like iron and its excellent electromagnetic absorption performance. *RSC Adv*. **2015**, *5*, 25936–25941.

[32] Qiang, R.; Du, Y. C.; Zhao, H. T.; Wang, Y.; Tian, C. H.; Li, Z. G.; Han, X. J.; Xu, P. Metal organic framework-derived Fe/C nanocubes toward efficient microwave absorption. *J. Mater. Chem. A* **2015**, *3*, 13426–13434.

[33] Lv, H. L.; Ji, G. B.; Zhang, H. Q.; Du, Y. W. Facile synthesis of a CNT@Fe@SiO_2 ternary composite with enhanced microwave absorption performance. *RSC Adv*. **2015**, *5*, 76836–76843.

[34] Zhao, B.; Shao, G.; Fan, B. B.; Zhao, W. Y.; Chen, Y. Q.; Zhang, R. Facile synthesis of crumpled ZnS net-wrapped Ni walnut spheres with enhanced microwave absorption properties. *RSC Adv*. **2015**, *5*, 9806–9814.

[35] Wen, S. L.; Liu, Y.; Zhao, X. C.; Cheng, J. W.; Li, H. Synthesis, dual-nonlinear magnetic resonance and microwave absorption properties of nanosheet hierarchical cobalt particles. *Phys. Chem. Chem. Phys*. **2014**, *16*, 18333–18340.

[36] Zhang, L. L.; Yu, X. X.; Hu, H. R.; Li, Y.; Wu, M. Z.; Wang, Z. Z.; Li, G.; Sun, Z. Q.; Chen, C. L. Facile synthesis of iron oxides/reduced graphene oxide composites: Application for electromagnetic wave absorption at high temperature. *Sci. Rep*. **2015**, *5*, 9298.

[37] Batter, B.; Wang, L.; Zhao, L.; Yu, P.; Tian, C. G.; Pan, K.; Fu, H. G. A novel Fe_3C/graphitic carbon composite with electromagnetic wave absorption properties in the C-band. *RSC Adv*. **2015**, *5*, 60135–60140.